Icarus **148**, 37–51 (2000)
doi:10.1006/icar.2000.6483, available online at http://www.idealibrary.com on IDEAL®

Radar Observations and Physical Model of Asteroid 6489 Golevka

R. S. Hudson

School of Electrical Engineering and Computer Science, Washington State University, Pullman, Washington 99164-2752
E-mail: hudson@eecs.wsu.edu

S. J. Ostro, R. F. Jurgens, K. D. Rosema,[1] J. D. Giorgini, R. Winkler, R. Rose, D. Choate, R. A. Cormier, C. R. Franck, R. Frye, D. Howard, D. Kelley, R. Littlefair, M. A. Slade, L. A. M. Benner, M. L. Thomas,[2] D. L. Mitchell,[3] P. W. Chodas, and D. K. Yeomans

Jet Propulsion Laboratory, California Institute of Technology, Pasadena, California 91109-8099

D. J. Scheeres

Department of Aerospace Engineering, The University of Michigan, 3048 FXB, Ann Arbor, Michigan 48109-2140

P. Palmer

Astronomy and Astrophysics Center, University of Chicago, 5640 South Ellis Avenue, Chicago, Illinois 60637

A. Zaitsev

Institute of Radioengineering and Electronics, Vedensky Square 1, 141120 Friazino, Russia

Y. Koyama

Communications Research Laboratory, Kashima Space Research Center, 893-1 Hirai, Kashima-Machi, Ibaraki 314, Japan

A. Nakamura

Graduate School of Science and Technology, Kobe University, 1-1 Rokkodai-cho, Nada-ku, Kobe, 657-8501, Japan

A. W. Harris

DLR Institute of Space Sensor Technology and Planetary Exploration Rutherfordstrasse 2, 12489 Berlin, Germany

and

M. N. Meshkov

Special Design Office, Moscow Energetic Institute, Krasnokazarmennaia 14, 111250 Moscow, Russia

Received February 21, 2000; revised April 20, 2000

We report 8510-MHz (3.5-cm) radar observations of the Earth-crossing asteroid (ECA) 6489 Golevka (1991 JX) obtained between June 3 and June 15, 1995, at Goldstone, the Very Large Array and the Evpatoria (Ukraine) and Kashima (Japan) radio antennas. One-dimensional Doppler spectra are used to estimate the object's convex hull, refine the ephemeris, and yield four possible pole directions. Three-dimensional modeling using two-dimensional delay-Doppler images and published lightcurves unambiguously defines the pole and reveals an extraordinarily angular shape with flat sides, sharp edges and corners, and peculiar concavities. The equivalent diameter of the object is 530 ± 30 m, with moments of inertia about the (long, intermediate, short) axes proportional to (1.00, 1.38, 1.39) ± 0.1. The asteroid's pole direction is $\lambda = 202 \pm 5^\circ$, $\beta = -45 \pm 5^\circ$, and its sidereal period is $P = 6.0289 \pm 0.0001$ h.

The asteroid's circular polarization ratio, SC/OC $= 0.23 \pm 0.02$, is lower than the average for radar-detected near-Earth asteroids and reveals only a modest degree of near-surface roughness at

[1] Current address: 5209 21st Ave. NE, Seattle WA 98105.
[2] Current address: Scriptics Corp., 2593 Coast Avenue, Mountain View, CA 94043.
[3] Current address: Space Sciences Laboratory, University of California, Berkeley, CA 94720-7450.

0019-1035/00 $35.00

scales near the 3.5-cm wavelength. However, the approximately Lambertian radar scattering law implies considerable surface roughness at larger scales. The asteroid's radar scattering law is modeled as $\rho \cos^n \theta$, with $\rho = 0.25 \pm 0.12$ and $n = 1.7 \pm 0.7$ giving an equivalent spherical albedo of 0.18 ± 0.09. This value is in the middle of the distribution of albedos of S-class asteroid's previously imaged by radar. The Hapke parameters describing the object's optical scattering properties are $w = 0.173 \pm 0.006$, $h = 0.024 \pm 0.012$, $B_0 = 1.03 \pm 0.45$, $g = -0.34 \pm 0.02$, and $\bar{\theta} = 20 \pm 5^\circ$. Both the optical and the radar scattering properties are consistent with those of a typical S-class asteroid.

Goldstone-VLA plane-of-sky images do not resolve the asteroid but do provide astrometry with uncertainties less than 0.1 arcsec. Integration of an orbit based on all available radar and optical astrometry shows that Golevka has an insignificant probability of collision with any planet during at least the next nine centuries.

We investigate Golevka's dynamical environment, assuming uniform density. Some areas of the surface are characterized by large enough slopes that we expect that they are exposed, solid, monolithic rock.

Key Words: **asteroids; radar.**

INTRODUCTION

Golevka was discovered in May 1991 at Palomar by E. F. Helin (Marsden 1991), 3 weeks before passing 0.036 AU from Earth. It was detected in June of that year at Arecibo and Goldstone (Ostro *et al.* 1991). In March 1995 Golevka was recovered at Siding Spring Observatory (Williams 1995) 3600 arcsec from the position predicted by an optical-only orbit, but only 5 arcsec from the position predicted from an orbit that includes the radar data from 1991. Golevka's orbit is close to the 3 : 1 mean-motion resonance with Jupiter and has a 3.995-year period.

The 1995 approach to 0.034 AU on June 9 provided an excellent opportunity for groundbased investigations. Mottola *et al.* (1997, hereafter M+97) conducted an extensive international campaign of optical photometry and infrared radiometry, obtaining estimates of the asteroid's sidereal spin period (6.0264 ± 0.002 h), pole direction ($\beta = 35 \pm 10^\circ$, $\lambda = 347 \pm 10^\circ$), and Hapke parameters. They used radiometric observations to estimate the asteroid's approximate dimensions as $0.35 \times 0.25 \times 0.25$ km. They concluded that it has a high visual geometric albedo (∼0.6) marking it as an unusual object and tentatively assigned a V classification.

Here we report radar observations conducted on June 3, 4, and 6–15, 1995 (Table I). Those observations and subsequent modeling reveal Golevka to be an unusually shaped object with surface properties fairly typical of an S-class asteroid.

OVERVIEW OF OBSERVATIONS

We observed Golevka with the Goldstone X-band (8510-MHz, 3.52-cm) system using a variety of radar configurations aimed at characterizing the object, refining its orbit, and establishing the technical feasibility of novel radar experiments. Goldstone's 70-m antenna, DSS-14, was used for all transmissions. On June 14 we conducted radar aperture-synthesis observations, with Goldstone transmitting and the VLA receiving. The resultant images yield plane-of-sky positions with uncertainties of a few hundredths of an arcsec.

On June 13–15 we carried out the first intercontinental radar astronomy experiments. These bistatic observations consisted of cw transmissions from Goldstone and reception at the Evpatoria (Ukraine) 70-m antenna on each of those dates (Zaitsev *et al.* 1997) and reception at the Kashima (Japan) 34-m antenna on

TABLE I
Experiment Overview

DOY	1995 Date	Start–Stop (hhmm–hhmm)	RA	Dec	Duration s	Duration RTT	SNR Date	SNR Run	Setups
154	June 3	0900–1200	3.0	235	17	45	340	20	cw rng
155	June 4	0930–1220	2.8	240	20	42	480	27	cw
156	June 5								
157	June 6	1015–1320	3.1	251	28	37	800	41	cw low
158	June 7	0750–1400	6.2	258	31	36	1000	50	cw G-V rng low
159	June 8	0750–1330	5.3	267	35	35	1200	55	Low high
160	June 9	0830–1515	6.7	277	38	34	1300	61	Low high
161	June 10	0830–1620	7.8	287	40	34	1300	61	Low high
162	June 11	0915–1645	7.5	299	40	36	1200	55	Low high
163	June 12	0910–1710	8.0	308	40	38	940	45	cw G-V low
164	June 13	0555–1717	11.3	317	39	41	690	35	cw G-E low high
165	June 14	0625–1755	11.5	324	38	44	570	29	cw G-E low high
166	June 15	0645–1755	11.2	331	37	47	390	21	cw G-E,K low high

Note. DOY is day of year, RA is right ascension, Dec is declination, and RTT is echo roundtrip time delay (equal numerically to the approximate distance in 10–3 AU). Predicted values of the echo's signal-to-rms-noise ratio (SNR) per date and the maximum SNR per run were based on conservative assumptions about the target and the radar system. Setups (see Table II) are abbreviated cw (continuous wave), rng (coarse-resolution ranging), low (low-resolution imaging), and high (high-resolution imaging). G-V, G-E, and G-K indicate observations that used cw transmissions from Goldstone (DSS-14) and reception of echoes at the VLA, Evpatoria, or Kashima (see text); in those experiments, we also received echoes at DSS-13.

June 15 (Koyama *et al.* 1995). We also attempted bistatic observations with reception at the Weilheim (Germany) 30-m antenna, but those were not successful. Throughout the bistatic experiments, we received echoes at DSS-13, the 34-m Goldstone antenna about 22 km from DSS-14.

Monostatic observations with DSS-14 used three different configurations: a cw (Doppler-only) setup with 0.5-Hz spectral resolution, a "low-resolution" delay-Doppler imaging setup with 0.25-μs × 1.0-Hz pixels, and a "high-resolution" imaging setup of $0.125\,\mu\text{s} \times 0.5\,\text{Hz}$ that placed more than 100 pixels on the asteroid. We completed several hundred transmit/receive cycles (runs) each setup. The asteroid's ∼6.0-h synodic rotation period was evident from comparison of the delay-Doppler image sequences from consecutive days. Poleward motion of the subradar latitude was apparent from contraction of the echo bandwidth after closest approach. Most of the Goldstone tracks were more than 6 h long, permitting very thorough orientational coverage of the asteroid.

Table II lists the key characteristics of our setups. (For a block diagram of the Goldstone radar system see Fig. 1 of Ostro *et al.* (1996). For a detailed description of observation strategies and data processing, see Ostro (1993).) Our cw observations used a frequency-switching technique identical to that described most recently by Ostro *et al.* (1992).

Our Goldstone-VLA observations used techniques described by de Pater *et al.* (1994). For the G-VLA portion of this work DSS-14 illuminated the object with a cw signal whose frequency was continually adjusted to compensate for Doppler shifts so that the return would arrive at the VLA at 8510 MHz. The VLA recorded the opposite-sense circular polarization (OC) return. At the time of the observations, the VLA was being reconfigured from the DnA-array to the A-array. On June 14, only 12 of the 24 antennas that provided useful data were in A-array locations. However, the longest baselines (36 km) were present so that full angular resolution could be obtained for a point-like source. (The VLA's finest frequency resolution, 384 Hz, is much too coarse for resolving Golevka echoes in frequency.) The VLA received echoes while tracking the position interpolated from JPL orbit solution 21. Approximately every 10 min, the phase of the array was calibrated by observing the astrometric calibration source $2203 + 317$ (positional uncertainty, $<0.002''$). The amplitude was calibrated with respect to 3C48, which was assumed to have a flux density of 3.27 Jy. We edited and calibrated the data with the AIPS reduction system, constructing images with the AIPS task IMAGR for each ∼20 min of data. To obtain the optimal combination of angular resolution and signal-to-noise ratio, we used the AIPS default robustness parameter, resulting in a $0.21'' \times 0.14''$ beamwidth at a position angle of 46°. The average position during each ∼20-min period was determined by fitting a Gaussian to the image. The average total flux density returned by Golevka was 1.80 ± 0.2 Jy.

TABLE II
Radar Setups

Baud		RP	Band		Δf	Looks/	Time/	COM	
ns	m	(μs)	N_{COH}	Hz	(Hz)	rec	rec	Col	Row
11,000	1650	1397.0	2	358	5.592	22	3.9	32	11.0
2,000	300	254.0	12	328	5.126	21	4.1	32	11.8
250	37.5	31.75	492	64	1.000	4	4.0	32	22.8
125	18.75	15.875	1970	32	0.500	2	4.0	32	34.8
			500	0.488	Varied	128			

Note. Each setup's time resolution (baud, Δt), code repetition period RP, unaliased frequency window Band, and frequency resolution Δf are given. The first three setups used repetitive, binary-phase-coded cw waveforms with a 127-element code to obtain time-delay resolution. NCOH is the number of RP-long time series of voltage samples coherently summed after decoding. Fourier analysis of an RP-long time series of voltages within any given range cell produces a power spectrum, and repetition of that process for each range bin produces a delay-Doppler image that is referred to as one look. The number of looks summed to produce a single data record was chosen so each record would be a 4-s integration. All our delay-Doppler setups produced power arrays with 64 frequency cells and 127 time-delay cells. The last two columns list the offset from (0, 0) in the recorded arrays that would contain echoes from a point target if the delay-Doppler ephemeris were perfect and no extra transmitter and receiver frequency offsets were used.

All pointing and delay-Doppler prediction ephemerides were generated at Goldstone with JPL's On-site Orbit Determination program (OSOD). For the most part, the experiment was executed as planned. Stefano Mottola, Gerhard Hahn, and their colleagues had determined the asteroid's spin period to within a few percent by April 1995 (Mottola *et al.* 1995), and their communication of this result at that time was enormously valuable in planning the radar experiment. Similarly, optical astrometry by a number of observers, including R. Stone and A. Monet at the U.S. Naval Observatory and A. Whipple at McDonald Observatory, ensured that the ephemerides used during the first radar runs would be quite accurate.

During the first four dates we established the asteroid's gross radar properties, dealt with system problems, and refined the ephemerides enough to guarantee that images taken around closest approach would not be smeared. The first few days showed echoes with bandwidths of order 10 Hz and delay depths of slightly more than 2 μs (300 m). Our ephemerides are referenced to the asteroid's center of mass (COM), so an error-free ephemeris would result in echo spectra that straddle the nominal Doppler prediction and delay-resolved images whose leading edge would arrive ahead of the nominal delay location by approximately the delay depth of the target. In reducing our initial astrometry, we assumed that the COM lagged the leading edge by 2.6 μs, slightly more than the images' delay depth, with a very conservative uncertainty of 2.0 μs. Our runs on the first few days showed echoes nearly centered on the nominal frequency and within several microseconds of the nominal delay. By June 8 we had an orbit (OSOD solution 21) that was extremely accurate: delay corrections during June 9–15 were all smaller than 1 μs. Between June 10 and June 15, the echo drifted by about 0.5 μs in delay, or 75 m in range. That is, the delay smear rate was about 0.6 m per hour, or 5 cm in 0.5 min, which was the longest integration time of any of our imaging runs. Thus delay smearing was negligible.

TABLE III
Goldstone–VLA Estimates of Golevka's Offsets from Orbit Solution No. 21

	Orbit Solution No. 21		Measured offset	
Time (TT)	RA	Dec	RA (s time)	DEC (sec arc)
10 05 45	21 49 36.0115	38 17 31.396	0.0173 ± 0.0004	0.315 ± 0.003
10 31 38	21 50 04.0505	38 16 07.847	0.0103 ± 0.0004	0.293 ± 0.004
10 55 54	21 50 30.2552	38 14 49.336	0.0103 ± 0.0005	0.290 ± 0.004
11 19 49	21 50 56.0030	38 13 31.790	0.0166 ± 0.0004	0.345 ± 0.005
11 46 46	21 51 24.9226	38 12 04.217	0.0142 ± 0.0005	0.308 ± 0.005

Our G-VLA images do not resolve the asteroid, but do provide estimates of positional offsets relative to JPL orbit solution 21 shown in Table III. The RA and DEC tabulated are geocentric apparent angles (expressed with respect to a coordinate system defined by the Earth's true-equator plane and equinox-of-date). The offsets in Table III were added to corresponding RA and DEC astrometric coordinates (that is, expressed with respect to the Earth's mean-equator plane and equinox of the J2000.0 epoch). The coordinate system of the resulting absolute angular measures was rotated from the initial solution 21 frame of the DE-245 planetary ephemeris into the modern DE-405 system (DE-405 is aligned to within 0.003 arcsec of the ICRF93/J2000.0 radio-frame coordinate system and 0.01 arcsec of the FK5/J2000 optical frame). The resulting absolute astrometric ICRF93/J2000.0 angles are summarized in Table IV.

ORBIT

The data in Table IV, along with 634 optical observations from 1991 April 15 through 1999 July 23 and 26 radar delay and 25 Doppler measurements, were simultaneously fit in a weighted least-squares sense to solve for six osculating orbital elements (Table V). At the asteroid's distance of 0.0438 AU, G-VLA noise values (Table IV) correspond to one standard-deviation uncertainties of between 900 and 2600 m in the two orthogonal plane-of-sky directions. Inclusion of the 1995 VLA data reduced orbital element uncertainties by ~40% at the 1999 solution epoch, with the exception of perihelion date (TP). Knowledge of that parameter was not substantially affected by the short-arc of VLA data. It appears that the VLA data, with realistic uncertainties, is roughly comparable in accuracy with the best traditional optical astrometry (i.e., when Hipparcos-based reference catalogs are used in the reductions). However, data-fit residuals show a statistically insignificant improvement with VLA data included. This is due in part the large amount of radar and other optical data.

Golevka is classified as a potentially hazardous asteroid by the Minor Planet Center. Currently available radar and optical astrometry permits very accurate integration of Golevka's orbit within a 1200-year window (Table VI) and shows that Golevka's collision probability with any planet is negligible for at least the next nine centuries. Also note that the discovery apparition was the closest approach to Earth since 1730 and our imaging experiment took advantage of the closest Earth approach until 2374.

RADAR IMAGES AND ANALYSIS OF SPECTRA

The delay-Doppler data files listed in Table VII contain frames that are 4-s integrations, that is, original data records. The bistatic cw files in Table VII contain spectra from 3-min integrations. Reduced data are normalized to the rms receiver noise and are tagged with information about the radar system, setup, receive epoch, and data processing.

Our finest-resolution images used a frequency resolution of 0.5 Hz. The corresponding spatial resolution depends on a km/Hz conversion factor,

$$\text{km/Hz} = \frac{P_{\text{syn}}}{4.13 \cos \delta}, \tag{1}$$

where P_{syn} is the synodic spin period in days and δ is the subradar latitude (Ostro *et al.* 1995). Golevka's pole direction (see below) resulted in conversion factors between 61 and 169 m/Hz. Therefore the "transverse" linear resolution ranged from 31 to 84 m. The rotational smearing per minute was less than 6 m.

Figure 1 shows summed spectra from sequences of cw and delay Doppler runs. The approximately twofold shrinkage in the echo bandwidth over the course of the experiment corresponds to the poleward motion of the subradar latitude. The 10-Hz

TABLE IV
Goldstone-VLA Astrometry

Date UTC	RA (hh mm ss)	DEC (deg mm ss)	RA noise	DEC noise	Coordinate
1995 06 14.419951574	21 49 45.8532	+38 18 52.956	0.06″	0.03″	Geocentric
1995 06 14.437926111	21 50 13.8978	+38 17 29.493	0.06″	0.04″	Geocentric
1995 06 14.454777962	21 50 40.1140	+38 16 11.082	0.08″	0.04″	Geocentric
1995 06 14.471386759	21 51 05.8795	+38 14 53.694	0.06″	0.05″	Geocentric
1995 06 14.490102037	21 51 34.8098	+38 13 26.198	0.08″	0.05″	Geocentric

TABLE V
Orbital Solutions

	Solution No. 57 (with VLA)	Solution No. 57-A (without VLA)
Eccentricity (e)	$0.59749744(73) \pm 14$	$0.59749744(23) \pm 23$
Perihelion distance (q)	$1.01186876(31) \pm 35$ AU	$1.01186877(53) \pm 56$ AU
Perihelion passage (T_p)	1999 Jun $22.880701(5840) \pm 7734$	1999 Jun $22.880701(9287) \pm 7786$
Long. asc. node (Ω)	$212.30119(843434) \pm 145046^\circ$	$212.30126(357562) \pm 251258^\circ$
Arg. of perihelion (ω)	$65.13896(140747) \pm 145345^\circ$	$65.13889(749021) \pm 251422^\circ$
Inclination (I)	$2.289385(3937) \pm 4287$	$2.289387(2095) \pm 7284$

Note. Golevka's heliocentric osculating orbital elements at Epoch 1999 Aug 10.0 (TT) (JD 2451400.5), estimated using the full data set (optical and delay-Doppler radar astrometry). The left column is the best solution, incorporating G-VLA data. The right-hand column, solution 57-A, excludes only the G-VLA data. Formal 1-standard-deviation uncertainties (in units of the parenthetical decimal places) are shown, illustrating the effect of G-VLA data. Elements are in the frame of the JPL planetary ephemeris DE-405 (ICRF93/J2000), a quasar-based radio-frame, generally within 0.01 arcsec of the optical FK5/J2000 frame. Angular orbital elements are referred to the ecliptic and mean equinox of J2000. Weighted r.m.s residuals for Solution 57 are 1.0 arcsec, 1.2 Hz (21 mm/s in radial velocity) and 0.51 μs in time delay (77 in range).

TABLE VI
Close Planetary Approaches

TDB close approach epoch					Distance	3-σ Uncertainty		Ellipse
Julian date	Year	Month	Day	Body	(AU)	AU	km	(sigmas)
2334088.97881	1678	Jun	1.47881	Earth	0.031620	0.00037	55351	1.26E7
2351666.74417	1726	Jul	18.24417	Earth	0.061737	0.00005	7480	1.59E7
2353057.61907	1730	May	9.11907	Earth	0.007248	<1.0E-5	<1496	1.83E5
2358804.52281	1746	Feb	1.02281	Mars	0.090168	<1.0E-5	<1496	3.70E6
2386666.76552	1822	May	16.26552	Earth	0.035767	<1.0E-5	<1496	1.40E5
2424728.99162	1926	Aug	1.49162	Mars	0.086428	<1.0E-5	<1496	3.57E6
2432009.91144	1946	Jul	8.41144	Mars	0.061663	<1.0E-5	<1496	2.38E6
2440939.84961	1970	Dec	19.34961	Mars	0.074595	<1.0E-5	<1496	4.33E6
2448419.30338	1991	Jun	11.80338	Earth	0.033185	<1.0E-5	<1496	1.59E8
2449877.59441	1995	Jun	9.09441	Earth	0.034106	<1.0E-5	<1496	7.53E7
2451332.31075	1999	Jun	2.81075	Earth	0.050052	<1.0E-5	<1496	2.13E7
2452780.17251	2003	May	20.67251	Earth	0.092265	<1.0E-5	<1496	6.79E6
2468479.72649	2046	May	14.22649	Earth	0.050800	<1.0E-5	<1496	2.29E6
2493777.85949	2115	Aug	19.35949	Earth	0.056411	<1.0E-5	<1496	3.47E6
2509468.83273	2158	Aug	4.33273	Earth	0.059561	<1.0E-5	<1496	2.96E6
2510891.46604	2162	Jun	26.96604	Earth	0.041460	<1.0E-5	<1496	1.01E7
2512322.17971	2166	May	27.67971	Earth	0.087832	<1.0E-5	<1496	7.33E6
2513786.99246	2170	May	31.49246	Earth	0.099166	<1.0E-5	<1496	1.22E7
2516802.95835	2178	Sep	2.45835	Mars	0.077759	<1.0E-5	<1496	2.46E6
2519641.02465	2186	Jun	10.52465	Earth	0.075611	<1.0E-5	<1496	4.40E7
2521106.07352	2190	Jun	14.57352	Earth	0.065573	<1.0E-5	<1496	4.49E7
2522594.54057	2194	Jul	12.04057	Earth	0.059846	<1.0E-5	<1496	5.32E6
2549257.19350	2267	Jul	12.69350	Earth	0.081388	<1.0E-5	<1496	5.29E6
2575591.34568	2339	Aug	18.84568	Earth	0.074582	<1.0E-5	<1496	2.07E6
2578320.03665	2347	Feb	6.53665	Mars	0.044432	<1.0E-5	<1496	1.34E6
2588378.51523	2374	Aug	22.01523	Earth	0.030735	<1.0E-5	<1496	1.70E6
2598236.15722	2401	Aug	17.65722	Earth	0.033865	<1.0E-5	<1496	1.75E6
2610930.41033	2436	May	19.91033	Mars	0.042254	0.00012	17952	1.18E6
2617888.56287	2455	Jun	8.06287	Earth	0.040112	0.00001	1496	8.99E6
2651442.94494	2547	Apr	21.44494	Mars	0.037813	<1.0E-5	<1496	8.56E5
2709618.97224	2706	Aug	2.47224	Earth	0.089030	0.00002	2992	2.55E4.
2710904.11200	2710	Feb	7.61200	Mars	0.052943	0.00006	8976	7.65E4
2718105.59150	2729	Oct	27.09150	Mars	0.017782	0.00007	10472	6.33E3
2727821.33807	2756	Jun	2.83807	Earth	0.047087	0.00007	10472	7.73E5
2737766.41869	2783	Aug	25.91869	Earth	0.032864	0.00123	184005	9.57E5
2774415.14899	2883	Dec	27.64899	Mars	0.022451	0.00119	178021	2.28E5

Note. Close approaches of Golevka to within 0.1 AU of inner Solar System bodies, along with 3-σ close-approach distance uncertainties. The asteroid remains more than 1 AU from Jupiter throughout this period. These formal uncertainties may underestimate true uncertainties by factors of several or more for encounters centuries away from the present, but give an indication of the span over which present observational data permits useful extrapolation. The final column gives the uncertainty ellipse that intersects the center of the planetary body in multiples of one standard deviation.

TABLE VII
Experiment Masterlog

File	μs	Hz	OSOD	OFF	CLT	LE	Runs	Start	Mid	Stop	P_T	Min
June 3												
154Acw	cw	0.488	14	None			5 (1–5)	0903	0908	0913		
15403	11	5.6	17	TX+50	11	10	19 (10–28)	1025	1042	1059	467	34
15406	2	5.1	17	TX+50	11.8	9	12 (30–41)	1116	1127	1139	467	23
154Bcw	cw	0.488	17	None			4 (42–45)	1155	1158	1201	467	6
June 4												
155cw	cw	0.488	17	None			20 (1–20)	0934	0952	1010	465	26
June 6												
157cw	cw	0.488	17	None			10 (1–10)	1016	1024	1031	470	15
15703	2	5.1	17	TX+50	11.8	13	10 (11–20)	1050	1059	1108	470	18
15706	0.25	1.0	17	TX+50	22.8	33	46 (21–66)	1133	1215	1258	400	25
15707	0.25	1.0	17	TX+50	22.8	33	6 (67–72)	1309	1314	1320	400	10
June 7												
158cwV	cw	0.488	17	RC-50			Bistatic	0800	0900	1000	470	120
15804	0.25	1.0	17	TX+15	22.8	45	29 (4–32)	1111	1145	1158	430	47
15805	0.25	1.0	17	TX+15	22.8	45	53 (33–85)	1212	1257	1342	430	90
15806	0.25	1.0	17	TX+15	22.8	45	5 (86–90)	1345	1349	1353	430	8
June 8												
15903	0.25	1.0	19	TX+15	22.8	28	7 (1–7)	0825	0831	0837	440	13
15904	0.25	1.0	19	TX+15	22.8	28	9 (13–21)	0917	0926	0934	440	6
15905	0.25	1.0	19	TX+15	22.8	28	40 (22–60)	0937	1119	1100	440	83
15908	0.125	0.5	19	None	34.8	46	50 (61–110)	1119	1205	1252	410	93
15909	0.125	0.5	19	None	34.8	46	21 (111–131)	1258	1314	1330	410	32
June 9												
16003	0.25	1.0	21	TX+15	22.8	15	35 (1–35)	0831	0902	0935	420	63
16006	0.125	0.5	21	None	34.8	22	53 (36–88)	1000	1045	1130	420	89
16007	0.125	0.5	21	None	34.8	22	53 (89–141)	1144	1225	1306	420	72
16008	0.125	0.5	21	None	34.8	22	54 (142–195)	1310	1358	1447	420	96
16009	0.125	0.5	21	None	34.8	22	15 (196–210)	1451	1502	1513	420	23
June 10												
16103	0.25	1.0	21	TX+15	22.8	15	29 (1–29)	0832	0854	0917	430	45
16106	0.125	0.5	21	None	34.8	20	30 (30–60)	0936	1002	1040	425	3
16111	0.125	0.5	21	None	34.8	20	49 (96–145)	1238	1320	1402	425	85
16112	0.125	0.5	21	None	34.8	20	53 (146–199)	1414	1501	1548	425	94
June 11												
16203	0.25	1.0	21	TX+15	22.8	15	8 (1–8)	0927	0936	0944	430	17
16204	0.25	1.0	21	TX+15	22.8	15	7 (9–15)	0947	0953	0958	430	10
16207	0.125	0.5	21	None	34.8	18	54 (16–69)	1012	1057	1141	425	88
June 12												
16303	0.25	1.0	21	TX+15	22.8	15	49 (1–49)	1430	1515	1600	450	90
June 13												
16403	0.25	1.0	21	TX+15	22.8	14	10 (1–10)	1335	1345	1355	435	23
16406	0.25	0.5	21	None	34.8	17	43 (11–53)	1407	1456	1545	429	97
June 14												
165AcwE				Blocked into 50 3-min sums				0636	0748	0900	474	16
165AcwV				Blocked into 50 3-min sums				0922	1041	1200	474	9
16503	0.25	1.0	21	TX+15	22.8	14	10 (1–10)	1229	1242	1255	450	6
16506	0.125	0.5	21	None	34.8	17	17 (11–27)	1308	1324	1340	450	31
165BcwK				Blocked into 50 3-min sums				1421	1607	1755	475	35
June 15												
166AcwE				Blocked into 50 3-min sums				0647	0816	0945	450	52
166BcwK				Blocked into 50 3-min sums				1524	1644	1755	450	43
16603	0.25	1.0	21	TX+15	22.8	13	44 (1–44)	1010	1120	1230	445	120
16606	0.125	0.5	21	None	34.8	17	48 (45–92)	1245	1336	1426	445	101
16607	0.125	0.5	21	None	34.8	17	16 (94–109)	1432	1447	1501	445	28

Note. This masterlog describes each useful data file obtained at Goldstone, in chronological order. The setup (see Table II) provided the indicated delay/Doppler resolution. The column labeled OSOD identifies the orbit solution used for the observation ephemerides. Some setups used transmitter or receiver frequency offsets to adjust the location of echoes within the frequency window. The offset is accounted for in the column labeled CLT, which gives the row (we count from zero) that would contain echoes from a point target if the delay-Doppler ephemeris were perfect. LE gives the row containing the echo's leading edge. P_T is transmitter power in kilowatts. The other columns are self-explanatory. All sequences used reception at DSS-14 except those with filenames flagged with E, V, or K, which used reception at DSS-13.

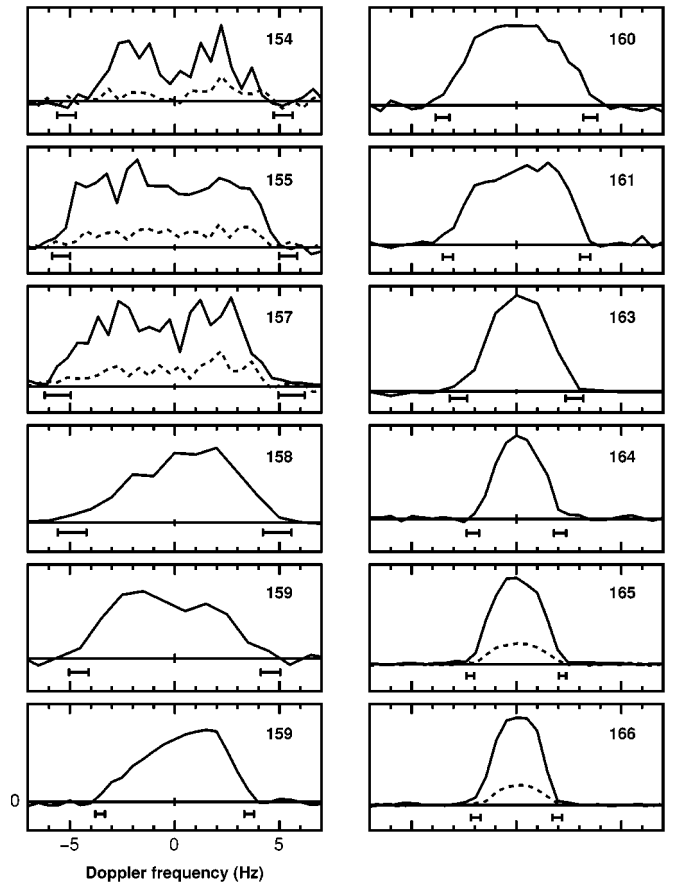

FIG. 1. Single-date sums of echo spectra from cw and delay-Doppler observations. OC spectra (solid curves) are available on all dates, and SC spectra (dashed curves) are available from cw sequences only. The vertical bar at 0 Hz indicates ±1 standard deviation. The two DOY-159 spectra correspond to high-resolution and low-resolution observations.

bandwidth of the June 4 (DOY 155) spectrum and the asteroid's synodic rotation period bound the maximum breadth of the asteroid's pole-on silhouette as

$$D \geq 600\,\mathrm{m}/\cos\delta. \qquad (2)$$

Table VIII lists estimates of the average OC radar cross section (σ_{oc}) and SC/OC ratio (μ_c) for individual dates and for the entire

TABLE VIII
Disc-Integrated Radar Properties

DOY	1995 Date	σ_{oc} (km^2)	μ_c
154	June 3	0.036	0.22
155	June 4	0.037	0.24
157	June 6	0.034	0.27
165	June 14	0.047	0.23
166	June 15	0.051	0.23
Average		0.040	0.23

Note. Uncertainties are ±50% in the radar cross section σ_{oc} and ±10% in the circular polarization ratio μ_c = SC/OC.

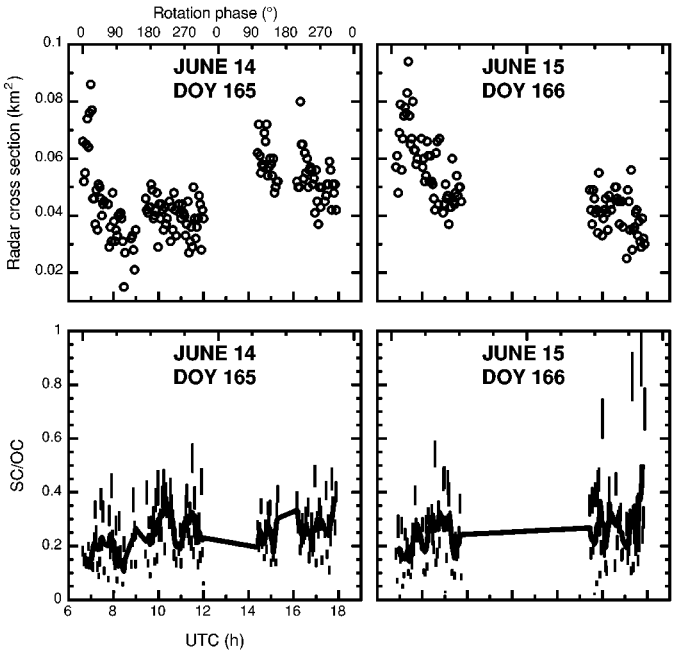

FIG. 2. Radar cross section (σ_{oc}) and polarization radio (μ_c = SC/OC) estimates from individual runs on June 14 and 15. The bars in the SC/OC plots span ±1 standard deviation. Much of the scatter in the cross section plots probably is due to variations in the antenna pointing accuracy.

experiment. Uncertainties in system parameters and trends in single-run estimates lead us to assign fractional errors of ±50% to the radar cross section estimate. The uncertainty in single-date values of μ_c is 10%. Fig. 2 plots estimates of OC cross section and SC/OC ratio from single runs. Figure 3 is a "movie" of the low- and high-resolution delay-Doppler with no attempt to incorporate km/Hz conversion factors.

Hull Estimation

We used June 14 and 15 cw spectra obtained at DSS-13 during the bistatic international experiments to estimate the convex envelope, or hull, of Golevka's pole-on silhouette (Ostro *et al.* 1988). Since the echo bandwidth decreased slightly between June 14 and June 15, we treated the two dates separately. For each date the phase coverage was excellent and more than adequate to define the hull's odd harmonics. We devoted much effort to evaluating the accuracy of edge-frequency estimators using simulations. Figure 4 shows our hull estimates and associated quantities.

The hull estimations yielded insignificant corrections to OSOD solution 21 predictions of f_{COM}: $+0.029 \pm 0.088$ Hz for June 14 and $+0.015 \pm 0.110$ for June 15; the assigned standard deviations are based on the shape of $\chi^2(f_{COM})$ near its minimum. Including the corresponding Doppler estimates (Table IX) in the orbital calculation produced a slightly refined orbit (OSOD-25), which we used to assign COM frequencies (shown as the origin in our figures) to our cw spectra.

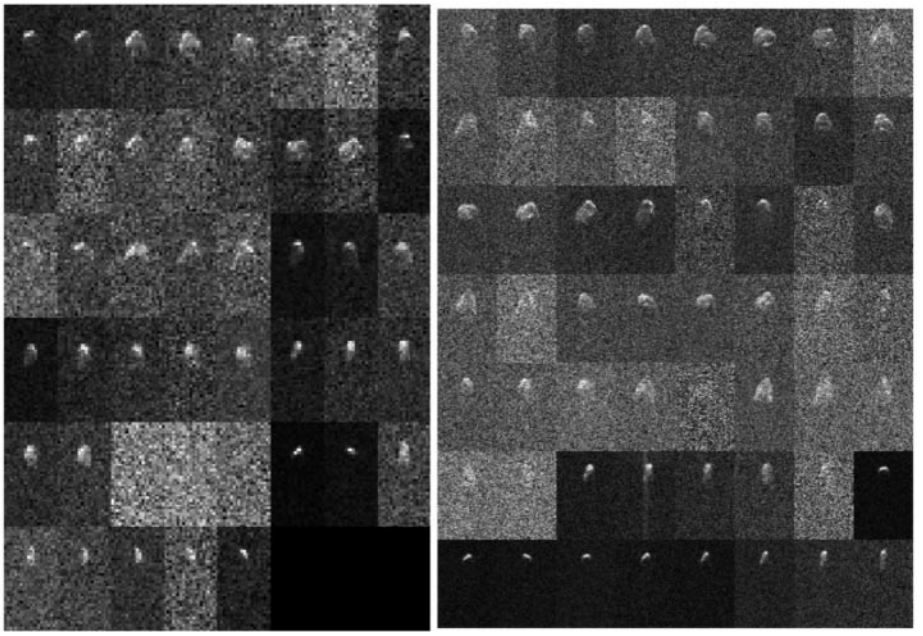

FIG. 3. The delay-Doppler image data set. (Left) 0.25-μs data; (right) is 0.125-μs data. Time increases left to right and top to bottom. Delay increases top to bottom. Doppler increases left to right. Raw Doppler scaling is used.

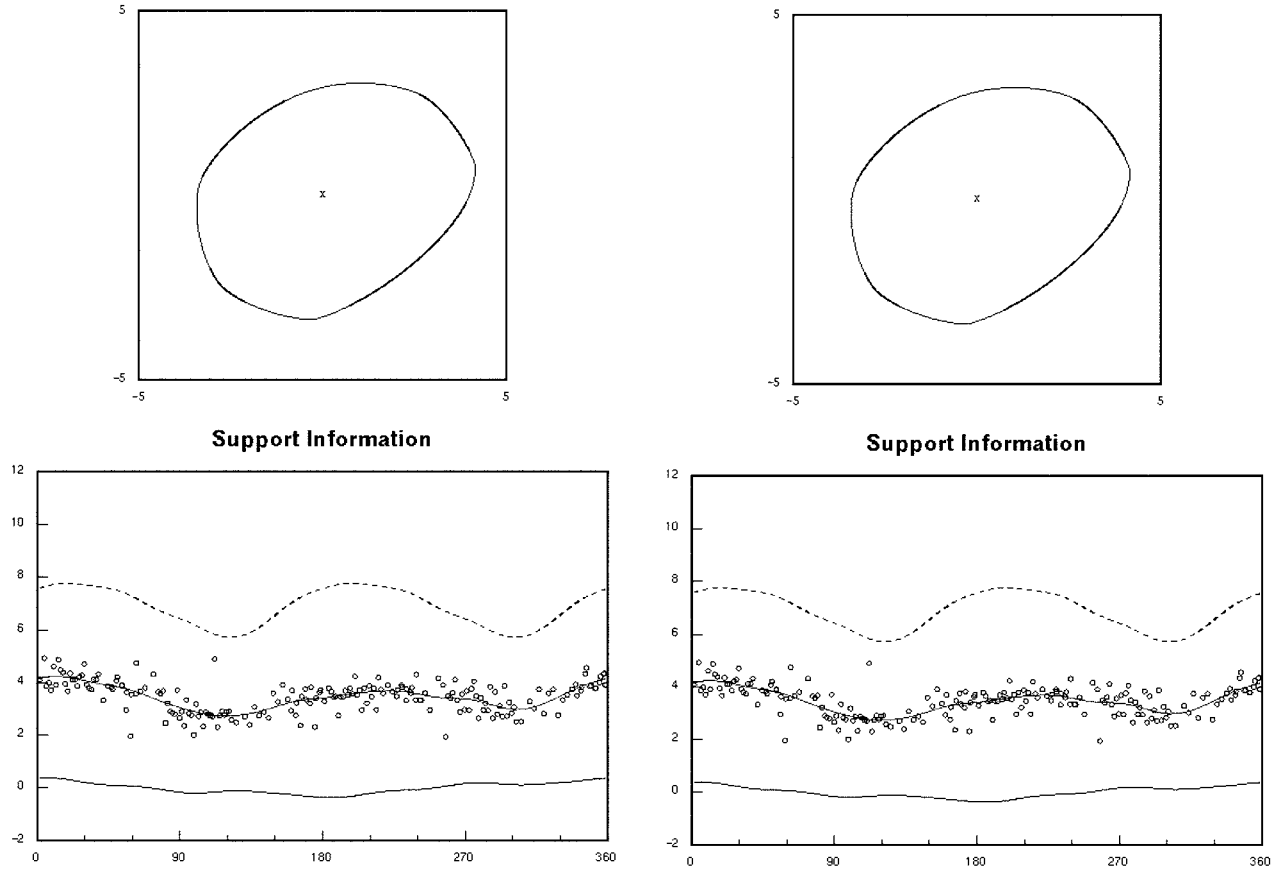

FIG. 4. Hulls estimated from June 14 and 15 (DOYs 165 and 166) and related quantities. (Top) Hull estimates. The X is the projected position of the asteroid's center of mass. Axes are in units of 0.488-Hz resolution cells. (Bottom) Related quantities, in units of 0.488-Hz resolution cells, are plotted vs rotation phase in degrees. Open circles are support function data; the middle curve is the model support function. The upper curve gives the hull's bandwidth, and the lower curve gives the hull's middle frequency.

TABLE IX
Goldstone Delay-Doppler Astrometry

Epoch (UTC)					
yyyy-mm-dd	hh:mm:ss	Data type	Estimate	Residual	Receive antenna
1995-06-03	11:30:00	Delay	44750315.10 ± 2.000 μs	-1.16 μs	DSS-14
1995-06-06	12:20:00	Delay	36530290.90 ± 2.000 μs	0.27 μs	DSS-14
1995-06-07	12:30:00	Delay	34966444.80 ± 2.000 μs	0.43 μs	DSS-14
1995-06-08	10:40:00	Delay	34163260.10 ± 2.000 μs	0.49 μs	DSS-14
1995-06-09	09:00:00	Delay	34026478.80 ± 0.200 μs	0.48 μs	DSS-14
1995-06-10	09:00:00	Delay	34629605.70 ± 0.200 μs	0.35 μs	DSS-14
1995-06-10	11:00:00	Doppler	-106307.22 ± 0.025 Hz	0.02 Hz	DSS-14
1995-06-11	09:50:00	Delay	36020406.00 ± 0.200 μs	0.27 μs	DSS-14
1995-06-12	15:10:00	Delay	38558455.80 ± 0.200 μs	0.24 μs	DSS-14
1995-06-13	13:50:00	Delay	41048867.40 ± 0.200 μs	0.04 μs	DSS-14
1995-06-14	12:00:00	Doppler	-316749.327 ± 0.090 Hz	0.02 Hz	DSS-13
1995-06-14	12:40:00	Delay	43951930.90 ± 0.200 μs	-0.37 μs	DSS-14
1995-06-15	11:30:00	Delay	47174607.70 ± 0.200 μs	-0.78 μs	DSS-14
1995-06-15	12:00:00	Doppler	-345961.504 ± 0.110 Hz	0.01 Hz	DSS-13

Note. Astrometry corresponds to 8510-MHz transmission from DSS-14, reflection from Golevka's COM, and reception at the indicated antenna. Each antenna's reference point is the intersection of the azimuth and elevation axes. Residuals are with respect to OSOD Solution 25. The range equivalent of 1 μs is 150 m and the radial velocity equivalent of 1 Hz is 18 mm/s.

The June 14 estimation yields bandwidth extrema ($B_{\max}$, $B_{\min}$) $= (4.44, 3.12) \pm 0.35$ Hz and $B_{\max}/B_{\min} = 1.43 \pm 0.06$, and the June 15 estimation yields ($B_{\max}$, $B_{\min}$) $= (3.79, 2.79) \pm 0.45$ Hz and $B_{\max}/B_{\min} = 1.36 \pm 0.34$. The assigned standard deviations are subjective and consider the sensitivity of the results to the edge-frequency estimator as well as the simulations mentioned above. We adopt the more precise June 14 value as our estimate of the elongation of the asteroid's pole-on silhouette, $D_{\max}/D_{\min} = 1.43 \pm 0.06$. This value agrees with the elongation, 1.4, of the M+97 ellipsoid model. Golevka's elongation is slightly below the mean, 1.6, of radar-derived elongations estimated for near-Earth asteroids.

Pole Estimation

Golevka's approximately 80° of sky motion during the radar observations provides substantial leverage for estimation of the asteroid's pole direction and size. We adopted the M+97 sidereal spin period, $P = 0.25110 \pm 0.00001$ days = 6.02640 ± 0.00024 h. For June 14 and 15 we used the $B_{\max}$ from the hull estimations as our bandwidth estimates. For the other dates estimated the bandwidth from sums of echo spectra and/or sums of delay-Doppler images with peak powers of at least 10σ. We included Goldstone–Evpatoria June 13, 14, and 15 spectral sums and the Goldstone–Kashima June 15 spectral sum. Spectra obtained at DSS-13 during the June 13 Goldstone–VLA observations suffered from a setup error; we used a bandwidth estimate obtained from inspection of those data for this calculation, but not for anything else.

For each spectral sum, we calculated the bandwidth at 5 and 20% of peak power and at the 1- and 2-σ levels. Then we defined the midpoint of the range spanned by those four values to be our bandwidth estimate, with an uncertainty equal to half that range. The peak powers of these sums ranged from 14σ to 41σ. Almost all our sums sampled phases (computed using trial poles at first and eventually using the least-squares solution) within 20° of a bandwidth maximum, that is, close enough to "see" $B_{\max}$. Two sums from the long imaging sequences on June 9 and 10 sampled both bandwidth maxima. Because of slight asymmetry in the hull's shape with respect to its COM, those sequences' sums are expected to yield echo bandwidths that are about 4% larger than $B_{\max}$; we reduced the corresponding inputs for the pole estimation accordingly. Similarly, the June 3 sums covered phases about 60° before a $B_{\max}$ orientation; based on the hull shape we increased their bandwidth measurements by 1.2.

We searched the χ^2 surface defined by weighted squared residuals between our bandwidth measurements and values predicted as a function of pole direction and $D_{\max}$. This search revealed four minima, and additional searches at 1° intervals showed them to lie at the directions in Table X with χ^2 values within 2% of each other.

TABLE X
Candidate Pole Solutions

Name	λ	β	χ^2	Sense
D1	335	25	16.0	Direct
D2	26	55	15.8	Direct
R1	155	-25	15.7	Retrograde
R2	206	-55	16.0	Retrograde

Note. These four candidate poles were identified from variation in echo bandwidth over the course of the experiment. Uncertainties in each estimate of λ, β are 6°. This analysis also produced an estimate of the maximum pole-on breadth, $D_{\max} = 610 \pm 80$ m. Inversion of all delay-Doppler data yielded refined constraints on these quantities. See text and Table XI.

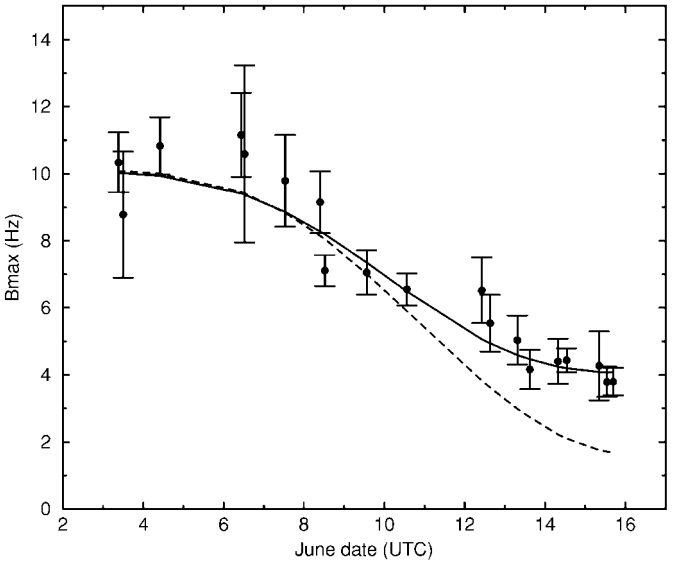

FIG. 5. Estimates of maximum echo bandwidth, $B_{\max}$, from cw data (see text). The solid curve corresponds to our four candidate pole directions and $D_{\max} = 0.61$ km; the dashed curve corresponds to the M+97 pole and $D_{\max} = 0.70$ km.

With 19 bandwidth measurements and three free parameters there are 16 degrees of freedom, and an increase in χ^2 by $\sqrt{2/16} = 35\%$ is statistically significant. This defines standard errors of 6° and 0.08 km in our least-squares estimates of pole direction and $D_{\max}$. Each solution is at $D_{\max} = 0.61$ km, and each predicts identical dependence of $|\delta|$ on each epoch. In particular, $|\delta|$ increased from 3° to 66° from June 3 to 15.

Figure 5 shows our $B_{\max}$ measurements and $B_{\max}$ predictions for our least-squares solution. We also show the predictions for the M+97 pole (347°, 35°) and $D_{\max} = 700$ m (the value needed to give a 10-Hz bandwidth on June 4). The factor by which $B_{\max}$ shrinks during June 3–15 is predicted to be 2.5 for the four poles in Table X. The Mottola *et al.* pole, only 14° away from ours, predicts a sixfold shrinkage (corresponding to a $|\delta|$ of 80° on June 15) that clearly is not observed. Each retrograde solution is paired with a direct solution 180° away from it. The acute angle between the lines defined by D1, R1 and D2, R2 is 48°.

PHYSICAL MODEL

Having constrained the pole-on silhouette and the pole direction using Doppler spectra, we proceeded to more detailed physical modeling using the delay-Doppler images. We followed the procedure described by Hudson and Ostro (1995, 1999).

Rotation-phase averaging was performed on the delay-Doppler images to increase the SNR to a level that we judged would support shape reconstruction. Ideally one would average over a range of phases small enough to avoid blurring at the edges of the images. For an object with maximum radius of 300 m and image resolution of 20 m, a point 300 m from the pole would migrate through no more than one resolution cell during 4° of rotation. For a rotation period of 6 h, this would be a 4-min window. Unfortunately, this amount of averaging did not produce sufficient SNR. We settled on a 20-min window as a compromise between SNR and blurring at the object's edges. Of course the blurring was less severe for the 0.25 μs (resolution about 40 m) images.

We first fit the full delay-Doppler data set with four models, each initialized to one of the four candidate pole solutions in Table X. Although so initialized, the spin states were free parameters in these fits. The objective function that we minimized (Hudson and Ostro 1994, 1995) included a weighted penalty term used to suppress nonsmoothness in the model, i.e., sharp edges and concavities. The weighting was increased until χ^2 rose significantly. (Given the number of degrees of freedom in the fit, a 1% change in χ^2 is significant.) The R1 and D2 models gave fits obviously worse than the D1 and R2 models. Both the D1 and R2 models could fit the data, but the D1 model did this with a smoother shape. For a non-smoothness-penalty weighting such that χ^2 of the D1 fit was just starting to rise significantly, the R2 χ^2 was 12% larger. This difference is statistically significant but visually the fits were not that different. Relaxing the smoothness constraint considerably allowed the R2 model to fit the data about as well as the D1 model, at the expense of a more irregular shape.

Given the very unusual Golevka lightcurves reported in M+97, we investigated how the D1 and R2 models might account for Golevka's optical properties. We digitized 67 data points from five of the more interesting M+97 lightcurves and included these data in our subsequent fits. We used a Hapke five-parameter photometric function to describe the optical scattering. We increased the model resolution to 1024 vertices and allowed the smoothness constraint to relax. We found that the D1 model could not account for both the radar and optical data, even qualitatively and even with rather tortured changes in shape. The R2 model, however, did give a simultaneous fit with relatively modest changes in shape. Therefore, of the four candidate poles in Table X, only the R2 solution led to a plausible fit to all the data and therefore is clearly selected by the modeling process. Numerical values from the fit are given in Tables XI and XII. Uncertainties are from a formal covariance matrix calculation.

Shape

Observed and modeled delay-Doppler images and the corresponding plane-of-sky appearance of the model are shown in Fig. 6. Lightcurves produced by the model corresponding to six of those shown in M+97 are shown in Fig. 7. Figure 6 reveals that Golevka has a shape dominated by large facets joined at relatively sharp edges. In some views (e.g., first row) it has an almost triangular silhouette. Several frames (e.g., last row) are dominated by a flat facet oriented almost normal to the radar. The corresponding delay-Doppler images show the unambiguous signature of this in the form of a collapse of the image in the delay dimension. Figure 8 shows the object rotated about both its long axis (top) and short axis (bottom). The model renderings

TABLE XI
Model Shape and Spin Parameters

Parameter	Definition	Value	Uncertainty
D_{eq}	Equivalent spherical diameter	530 m	30 m
D_{long}	Max extent along long axis of inertia	685 m	30 m
D_{int}	Max extent along intermediate axis of interia	489 m	30 m
D_{short}	Max extent along short axis of inertia	572 m	30 m
I_{short}/I_{long}	Moment of inertia ratio short-to-long axes	1.39	0.1
I_{int}/I_{long}	Moment of inertia ratio intermediate-to-long axes	1.38	0.1
λ	Ecliptic longitude of pole	202°	5°
β	Ecliptic latitude of pole	−45°	5°
P	Sidereal spin period	6.0289 h	0.0001 h

TABLE XII
Surface Properties

Parameter	Definition	Value	Uncertainty
ρ	Normal radar reflectivity	0.25	0.12
n	Specularity parameter	1.7	0.7
σ_{sp}	Equivalent spherical albedo (OC)	0.18	50%
μ_c	Circular polarization ratio	0.23	0.02
w	Particle single-scattering albedo	0.173	0.006
h	Opposition surge width	0.024	0.012
B_0	Opposition surge amplitude	1.03	0.45
g	Asymmetry parameter	−0.34	0.02
$\bar{\theta}$	Macroscopic roughness	20°	5°
p_v	Geometric albedo	0.151	0.023

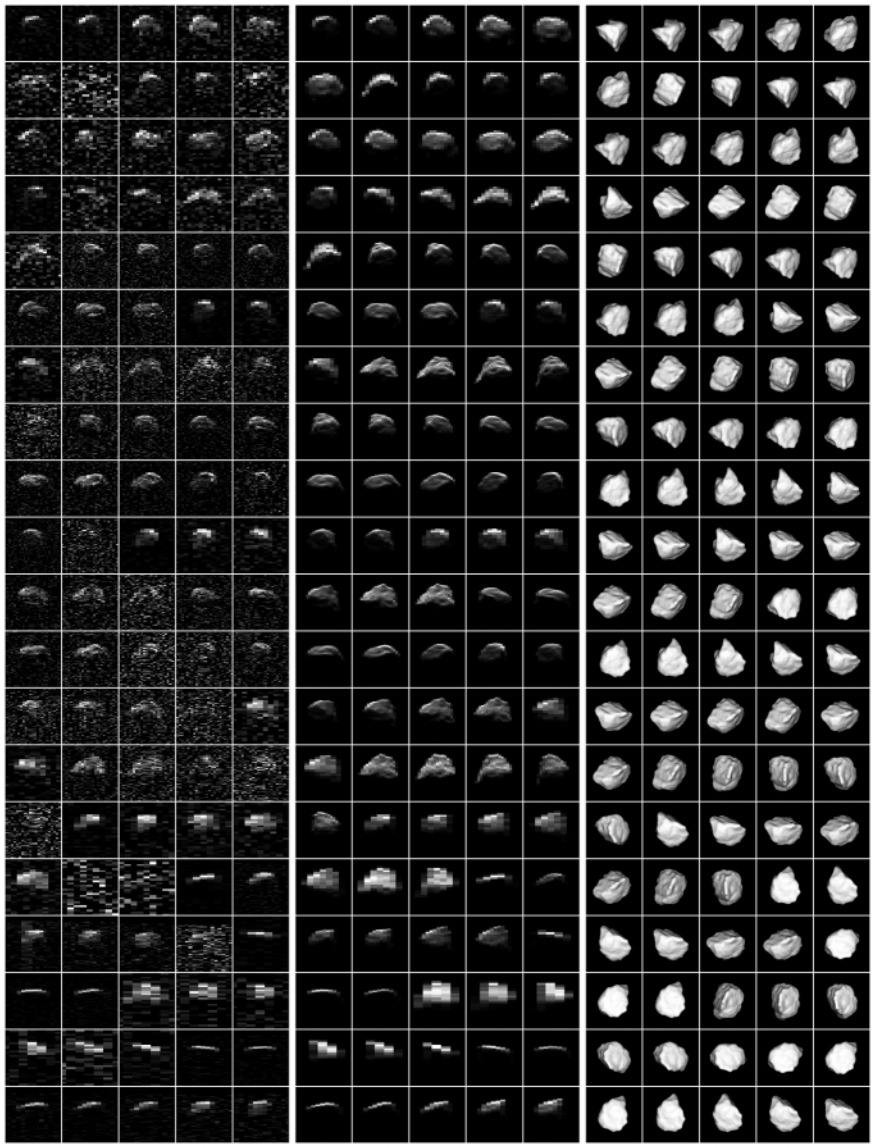

FIG. 6. One hundred observed (left) and modeled (center) delay-Doppler images and corresponding plane-of-sky appearance (right) of model with zero phase illumination and Lambertian scattering law. Both delay and Doppler axes have been scaled so that each frame is 1 km on a side.

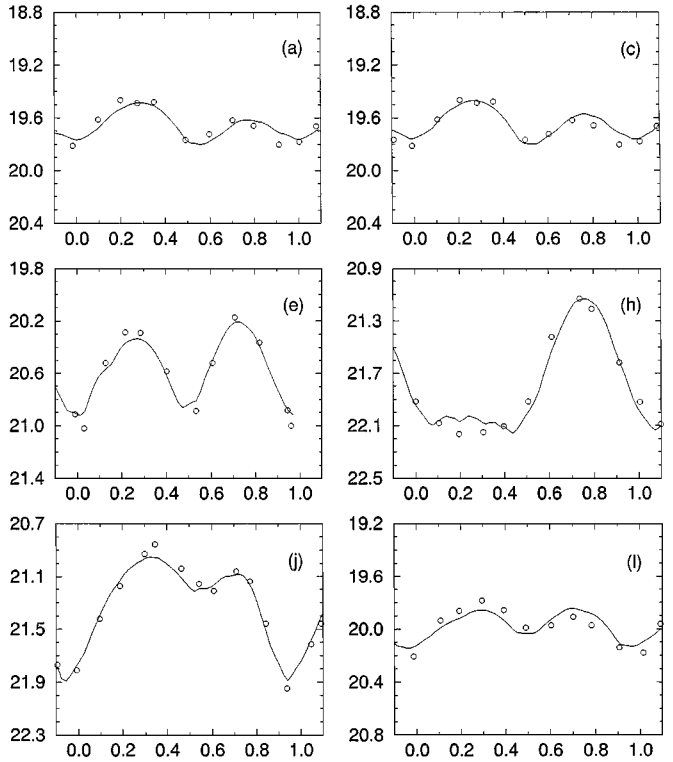

FIG. 7. Modeled lightcurves corresponding to Fig. 2 in M+97. The abscissa is relative rotation phase. The rms residual of the fits is 0.05 mag.

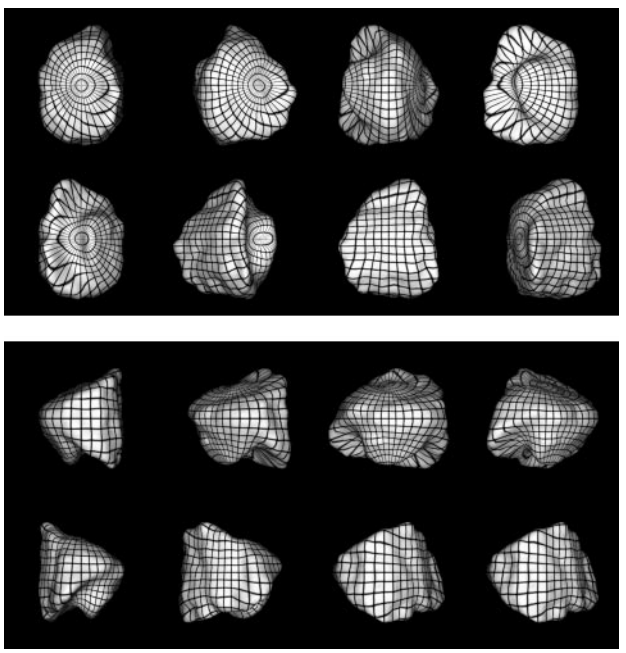

FIG. 8. Golevka model rotated in 45° steps about its long axis (top) and short axis (bottom). Dark lines show latitude and longitude in 10° increments. The first image in the top frame is from above the north pole, defined using the right-hand rule. In the bottom frame the north pole points up.

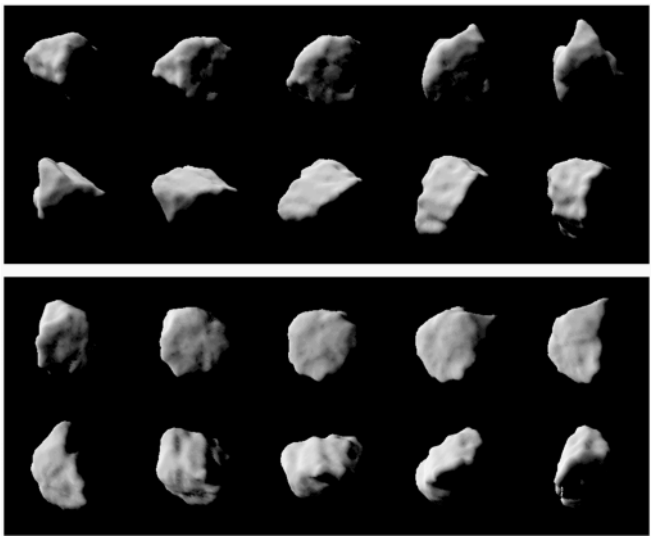

FIG. 9. Plane-of-sky appearance of Golevka model corresponding to (h) (top panel) and (j) (bottom panel) of Fig. 10. The model rotates by 0.1 rotation between frames, corresponding to abscissas 0.0 to 0.9 in Fig. 10.

of Figs. 6 and 8 also reveal a dramatic concavity that creates an almost finger-like appearance in some views.

Figure 9 shows renderings of the model with its orientation and illumination corresponding to frames (h) and (j) of Fig. 7. M+97 noted that, "a striking feature in the lightcurves is the progressive dimming of what, during the pre-close approach observations, was the primary maximum until its complete disappearance in the lightcurve of June 11." We see from these renderings that the prominent concavity is responsible for the disappearance of the primary lightcurve maximum in frame (h). Rotation of the flat facet on the opposite side in and out of the Sun's illumination is responsible for the almost single-minimum lightcurve in (j). The large-scale shadowing of Golevka's intricately nonconvex shape offers an explanation for the large slope of the asteroid's lightcurve amplitude vs solar phase angle (the amplitude-phase relation), as anticipated by M+97.

The shape model in Fig. 8 (short-axis rotation sequence, top left) resembles a normal fault block that is rotated clockwise by 90° and bounded by conjugate fault planes on the north and south. The north and south faces form angles between 55° and 70° relative to the vertical that are consistent with the dips of terrestrial normal faults (Suppe 1985) and with the distribution of fracture dip angles seen among fragments from hypervelocity laboratory impact experiments with free-falling concrete ellipsoids (Bianchi *et al.* 1984). Thus, it seems possible that Golevka was formed as a block in a normal fault and was subsequently dispersed from its parent body, perhaps by a catastrophic disruption.

Surface Properties

Golevka's mean absolute visual magnitude, $H = 19.079 \pm 0.029$ (M+97), is related to its visual geometric albedo p_v and

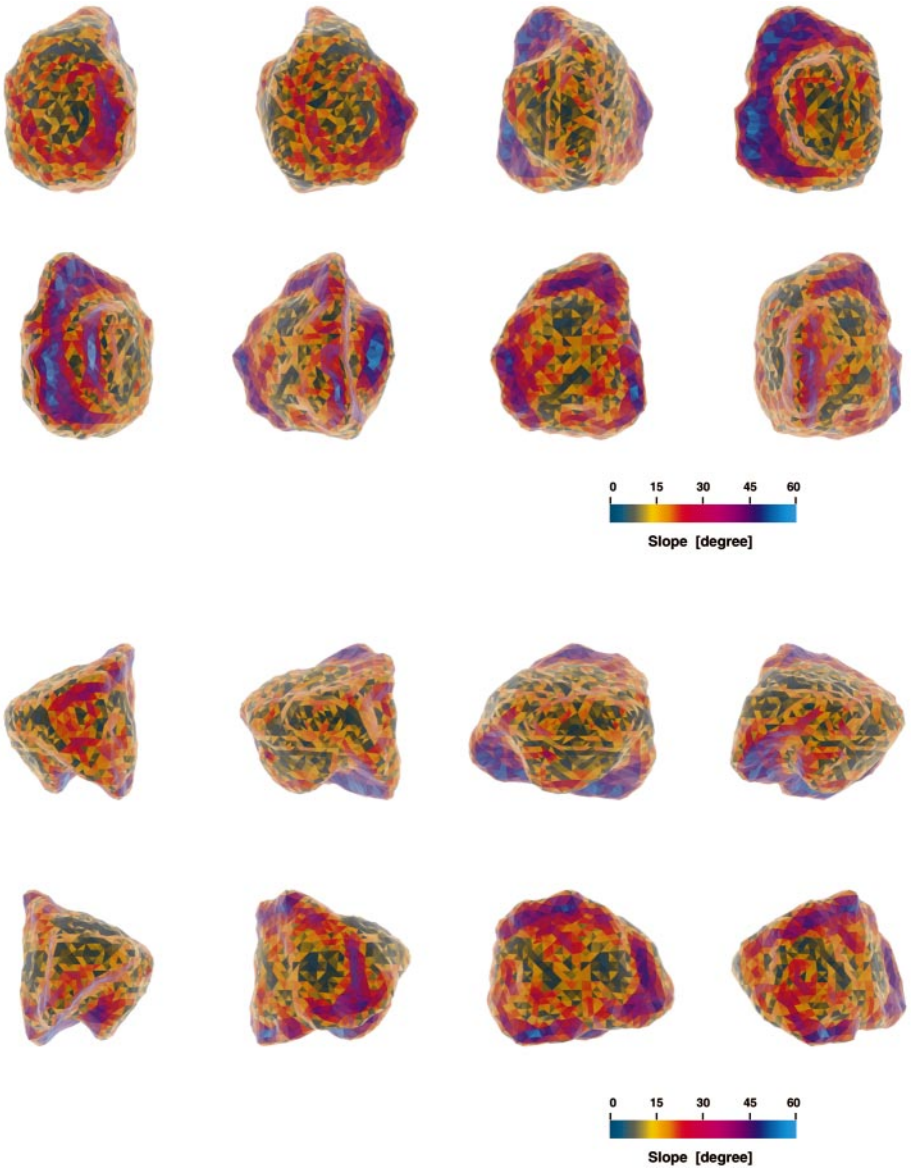

FIG. 10. Gravitational slopes over the surface of Golevka, computed for a density of 5 g/cm^{-3}. The slopes range up to a maximum of 60°.

its effective spherical diameter $D_{\rm eff}$ via the equation (Bowell *et al.* 1989)

$$\log p_{\rm v} = 6.259 - 2\log D - 0.4H.$$

Our value of $D_{\rm eff}$, 530 ± 30 m, yields $p_{\rm v} = 0.151 \pm 0.023$.

Hicks and Grundy (1995) interpreted their 0.55- to 1.05-μm reflectance spectra as evidencefor V classification. Hicks *et al.* (1998) argued that Golevka's broad 0.9- to 1.0-μm absorption, which is shallower and broader than Vesta's, could indicate the presence of some olivine. Hicks *et al.* (1999) report Golevka spectra with deep 1 and 2 μm absorptions consistent with a pyroxene rich surface suggested by the 0.5- to 1-μm spectra obtained in 1995. However, recent spectra are also consistent with an S classification (M. D. Hicks, pers. commun.). Indeed, our estimate of $p_{\rm v}$ is close to the mean of S asteroid values (0.18) but much lower than Vesta's (0.34) calculated using the Thomas *et al.* (1997) value for $D_{\rm eff}$.

Our results for Golevka's size, $p_{\rm v}$, spectral class, and Hapke parameters (Table XII) are irreconcilable with those of M+97, who obtain $D_{\rm eff} = 300$ m, $p_{\rm v} \sim 0.6$, and Hapke parameters ($\bar{\theta} = 7 \pm 7°$, $g = -0.435 \pm 0.001$, $w = 0.58 \pm 0.03$, $h = 0.0114 \pm 0.0004$, $B_0 = 0.758 \pm 0.014$). Because our size estimate is based on spatially resolved images, it should be more accurate than M+97's inferences from disc-integrated observations. The disparate VIS/IR estimates almost certainly are due to the fact that the models used in the M+97 analyses do not accommodate shapes nearly as irregular as Golevka's. The Standard Thermal Model (STM) and the Fast Rotating Model used to interpret their radiometry assume spheres, and the inaccuracy of those

models in this case, even when modified to deal with latitude and phase-angle effects, should be taken as a warning of the danger of applying them to extremely nonspherical objects. It is desirable that simulations be undertaken, perhaps using the Golevka shape model, to understand the thermal signatures of highly irregular shapes and to seek shape-dependent systematic errors. Brown's (1985) study of the thermal signatures of ellipsoids and Harris's (1998) modification of the STM are steps in this direction. As for the estimation of Hapke parameters from disc-integrated photometry, M+97 warned that "effects introduced by the irregular shape of the body are difficult to predict," and Hudson and Ostro (1998) demonstrated the value of an a priori shape model to such estimation.

Golevka's circular-polarization ratio $\mu_c = 0.23$ is lower than the mean of NEA values (mean 0.36, range 0.07 to 1.10) and indicates that most of the echo power is due to single scattering. The asteroid's OC radar albedo (OC radar cross section divided by projected area of a sphere with $D = 530$ m), $0.18 \pm 50\%$, is in the top half of the distribution of radar albedos for S asteroids (mean 0.14, range 0.04 to 0.32). The equivalent spherical albedo (that is, the albedo of a sphere with Golevka's radar scattering properties) would have the same value. Following Ostro *et al.* (1999) and references therein, we find that the average bulk density of the smooth component of Golevka's surface is no greater than 3.7 g cm^{-3}.

GOLEVKA'S DYNAMICAL ENVIRONMENT

Golevka's shape constrains its gravitational environment, and hence the dynamics of orbits close to it, which in turn have implications for the systematics of ejecta distribution, satellite stability, and operation of robotic or piloted spacecraft. Following Scheeres *et al.* (1998, 1996), we have assumed that Golevka's density is uniform, and have calculated the gravitational field (Werner and Scheeres 1997) for bulk densities between 2 and 5 g cm^{-3}. That range encompasses solid and 0.5-pore-fraction assemblages of stony iron, or ordinary chondritic assemblages. It also is consistent with surface density constraints implied by Golevka's radar properties.

Figure 10 shows the surface's distribution of gravitational slope (that is, the acute angle a plumb line would make with the local surface normal). The figure is calculated for a density of 5 g cm^{-3} but the slopes' density dependence in the pertinent interval is not significant. Slopes range from 0° to 60°. Tangential (along surface) accelerations on the steepest slopes are 0.25 mm s^{-2} for a density of 5 g cm^{-3}, and are proportional to the assumed density. Loose material is unlikely to exist on very steep slopes, and we expect that surfaces sloped as steeply as about 45° will consist of exposed solid, monolithic rock.

The minimum launch speed needed to guarantee that a particle will escape immediately from Golevka into heliocentric orbit varies over the surface, ranging from 16 to 36 cm s^{-1} for a density of 2 g cm^{-3} and from 31 to 57 cm s^{-1} for a density of 5 g cm^{-3}. The maximum launch speed for which a particle will

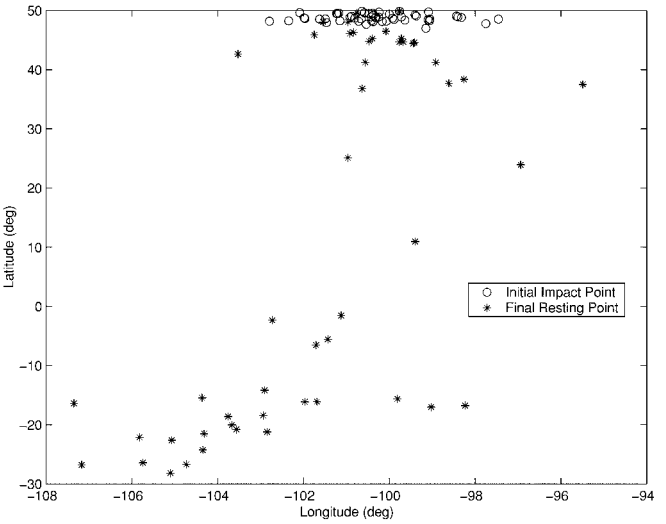

FIG. 11. Latitude and longitude of initial impact location and final resting location for 50 particles dropped above Golevka. Each particle was dropped with no initial velocity. The initial location of the particles were drawn from a Gaussian distribution centered at a 10-m altitude with a standard deviation of 5 m.

definitely return to the surface (regardless of launch direction) also varies over the surface, ranging from 2 to 17 cm s^{-1} for a density of 2 g cm^{-3} and from 20 to 35 cm s^{-1} for a density of 5 g cm^{-3}. In the interval between these two speeds, numerical integration is needed to determine the fate of a launched particle; the width of this interval varies over the surface, ranging from 7 to 24 cm s^{-1} for a density of 2 g cm^{-3} and from 8 to 26 cm s^{-1} for a density of 5 g cm^{-3}.

A piece of impact ejecta that returns to the surface can bounce many times, depending on the coefficient of restitution between the surface and ejecta. The path the particle follows on a small, irregularly shaped asteroid can be complex. For example, we have calculated the trajectories of 50 test particles dropped from within a small region above Golevka's surface. Their initial impact locations are clustered together, but their final resting sites are widely distributed over the surface (Fig. 11).

A particle orbiting Golevka will be stable against removal by solar gravitational perturbations within an "orbital zone" whose size is two times larger for retrograde orbits than for direct orbits (Hamilton and Burns 1992). For nearly circular orbits about Golevka, retrograde orbits are bound out to radii of 44 km for a density of 2 g cm^{-3} and 61 km for a density of 5 g cm^{-3}; corresponding limits for nearly circular direct orbits are half as large. The motion of a particle orbiting closer than ∼1 km may be made unstable by the nonspherical portion of the gravity field. For very small particles, perturbations from solar radiation pressure must be taken into account (Scheeres and Marzari 2000).

CONCLUSION

Our experiment reveals Golevka to have disc-integrated radar and optical surface properties fairly typical of an S-class asteroid,

but a shape that is highly angular and faceted. The harsh angularity of the shape seems inconsistent with this object being an unconsolidated agglomerate of particulate material bound just by gravity. Instead, it gives the impression of being a collision fragment.

Golevka is the first sub-kilometer object studied in this much detail, so we have no way of knowing how typical its shape is among half-kilometer-sized objects in the Solar System. This situation will change: improvements in the Goldstone and Arecibo telescopes and increases in the NEA discovery rate should provide a growing sample of sub-kilometer asteroids for which radar-based shape reconstructions are available.

ACKNOWLEDGMENTS

Work at Washington State University was supported, in part, by a grant from NASA. Part of this research was conducted at the Jet Propulsion Laboratory, California Institute of Technology, under contract with NASA. Work at University of Chicago was supported by NASA Grant NAG5-4292 to the University of Illinois and the University of Chicago. Work at University of Michigan was supported by NASA Grant NAGW-9017. The authors thank M. Belton and D. Simonelli for helpful reviews.

REFERENCES

Bianchi, R., F. Capaccioni, P. Cerroni, M. Coradini, E. Flamini, P. Hurren, G. Martelli, and P. N. Smith 1984. Experimental simulation of asteroid fragmentation by macroscopic hypervelocity impacts against free-falling bodies. *Astron. Astrophys.* **139**, 1–6.

Bowell, E., B. Hapke, D. Dominque, K. Lumme, K. Peltomiemi, and A. W. Harris 1989. Application of photometric models to asteroids. In *Asteroids II* (R. P. Binzel, T. Gehrels, and M. S. Mathews, Ed.), pp. 524–556. Univ. of Arizona Press, Tucson.

Brown, R. H. 1985. Ellipsoidal geometry in asteroid thermal models: The standard radiometric model. *Icarus* **131**, 291–301.

de Pater, I., P. Palmer, D. L. Mitchell, S. J. Ostro, D. K. Yeomans, and L. E. Snyder 1994. Radar aperture synthesis observations of asteroids. *Icarus* **111**, 489–502.

Hamilton, D. P., and J. A. Burns 1992. Orbital stability zones about asteroids II. *Icarus* **96**, 43–64.

Harris, A. W. 1998. A thermal model for near-earth asteroids. *Icarus* **131**, 291–301.

Hicks, M., and W. Grundy 1995. 1991 JX. *IAU Circ.* 6177.

Hicks, M. D., U. Fink, and W. M. Grundy 1998. The unusual spectra of 15 near-earth asteroids and extinct comet candidates. *Icarus* **133**, 69–78.

Hicks, M. D., M. S. Hanner, D. L. Rabinowitz, B. J. Buratti, T. L. Hayward, U. Fink, and W. Grundy 1999. 6489 Golevka revisited: New evidence for a pyroxene-rich near-Earth asteroid. *Bull. Am. Astron. Soc.* **31**, 1072.

Hudson, R. S., and S. J. Ostro 1994. Shape of asteroid 4769 Castalia (1989 PB) from inversion of radar images. *Science* **263**, 904–943.

Hudson, R. S., and S. J. Ostro 1995. Shape and non-principal axis spin state of asteroid 4179. *Science* **270**, 84–86.

Hudson, R. S., and S. J. Ostro 1998. Photometric properties of asteroid 4179 Toutatis from lightcurves and a radar-derived physical model. *Icarus* **135**, 451–457.

Hudson, R. S., and S. J. Ostro 1999. Physical model of asteroid 1620 Geographos from radar and optical data. *Icarus* **140**, 369–378.

Koyama, Y., and 18 colleagues 1995. Radar observations of an asteroid 1991JX. In *Proceedings for the 28th ISAS Lunar and Planetary Symposium*, pp. 201–204. ISAS, Japan.

Marsden, B. 1991. *IAU Circ.* 5268.

Mottola, S., and 24 colleagues 1995. Physical model of near-Earth asteroid (6489) 1991 JX from optical and infared observations. *Bull. Am. Astron. Soc.* **27**, 1055.

Mottola, S. A., and 27 colleagues 1997. Physical model of near-earth asteroid 6489 Golevka (1991 JX) from optical and infrared observations. *Astron. J.* **114**, 1234–1245.

Ostro, S. J. 1993. Planetary radar astronomy. *Rev. Mod. Phys.* **65**, 1235–1279.

Ostro, S. J., R. Connelly, and L. Belkora 1988. Asteroid shapes from radar echo spectra: A new theoretical approach. *Icarus* **73**, 15–24.

Ostro, S. J., J. K. Harmon, A. A. Hine, P. Perillat, D. B. Campbell, J. F. Chandler, I. I. Shapiro, R. F. Jurgens, and D. K. Yeomans 1991. High-resolution radar ranging to near-Earth asteroids. *Bull. Am. Astron. Soc.* **23**, 1144.

Ostro, S. J., and 11 colleagues 1992. Europa, Ganymede, and Callisto: New radar results from Arecibo and Goldstone. *J. Geophys. Res.* **97**, 18,227–18,244.

Ostro, S. J., and 13 colleagues 1995. Radar images of asteroid 4179 Toutatis. *Science* **270**, 80–83.

Ostro, S. J., R. F. Jurgens, K. D. Rosema, R. S. Hudson, J. D. Giorgini, R. Winkler, D. K. Yeomans, D. Choate, R. Rose, M. A. Slade, S. D. Howard, D. J. Scheeres, and D. L. Mitchell 1996. Radar observations of asteroid 1620 Geographos. *Icarus* **121**, 44–66.

Ostro, S. J., and 15 colleagues 1999. Asteroid 4179 Toutatis: 1996 radar observations. *Icarus* **137**, 122–139.

Scheeres, D. J., and F. Marzari 2000. Temporary orbital capture of ejecta from comets and asteroids: Application to the Deep Impact experiment. *Astron. Astrophys.* **356**, 747–756.

Scheeres, D. J., S. J. Ostro, R. S. Hudson, and R. A. Werner 1996. Orbits close to asteroid 4769 Castalia. *Icarus* **121**, 67–87.

Scheeres, D. J., S. J. Ostro, R. S. Hudson, E. M. DeJong, and S. Suzuki 1998. Dynamics of orbits close to asteroid 4179 Toutatis. *Icarus* **132**, 53–79.

Suppe, J. 1985. *Principles of Structural Geology*, p. 293. Prentice-Hall, Englewood Cliffs, NJ.

Thomas, P. C., R. P. Binzel, M. J. Gaffey, A. D. Storre, E. N. Wells, and B. H. Zellner 1997. Impact excavation on asteroid 4 Vesta: Hubble Space Telescope results. *Science* **277**, 1492–1495.

Werner, R. A., and D. J. Scheeres 1997. Exterior gravitation of a polyhedron derived and compared with harmonic and Mascon gravitation representations of asteroid 4769 Castalia. *Celest. Mech. Dynam. Astron.* **65**, 313–344.

Williams, G. V. 1995. *M.P.E.C.* 1995-F04.

Zaitsev, A. L., and 24 colleagues 1997. Intercontinental bistatic radar observations of 6489 Golevka (1991 JX). *Planet. Space Sci.* **45**, 771–778.